Extrinsic self-calibration of an operational mobile LiDAR system

Axel L. Diehm, Joachim Gehrung, Marcus Hebel*, Michael Arens
Fraunhofer IOSB, Ettlingen, Fraunhofer Institute of Optronics, System Technologies and Image
Exploitation, Gutleuthausstr. 1, 76275 Ettlingen, Germany

ABSTRACT

In this paper, we describe a method for automatic extrinsic self-calibration of an operational mobile LiDAR sensing system (MLS), that is additionally equipped with a POS position and orientation subsystem (e.g., GNSS/IMU, odometry). While commercial mobile mapping systems or civil LiDAR-equipped cars can be calibrated on a regular basis using a dedicated calibration setup, we aim at a method for automatic in-field (re-)calibration of such sensor systems, which is even suitable for future military combat vehicles. Part of the intended use of a mobile LiDAR or laser scanning system is 3D mapping of the terrain by POS-based direct georeferencing of the range measurements, resulting in 3D point clouds of the terrain. The basic concept of our calibration approach is to minimize the average scatter of the 3D points, assuming a certain occurrence of smooth surfaces in the scene which are scanned multiple times. The point scatter is measured by local principal component analysis (PCA). Parameters describing the sensor installation are adjusted to reach a minimal value of the PCA's average smallest eigenvalue. While sensor displacements (lever arms) are still difficult to correct in this way, our approach succeeds in eliminating misalignments of the 3D sensors (boresight alignment). The focus of this paper is on quantifying the influence of driving maneuvers and, particularly, scene characteristics on the calibration method and its results. One finding is that a curvy driving style in an urban environment provides the best conditions for the calibration of the MLS system, but other structured environments may still be acceptable.

Keywords: Mobile laser scanning, MLS, LiDAR, 3D mapping, direct georeferencing, calibration, sensor alignment

1. INTRODUCTION

Mobile laser scanning or, more generally, mobile LiDAR sensing (MLS) is an established 3D sensing technology on the civil market. For instance, prototypes of self-driving cars typically rely on LiDAR sensor data, and mobile laser scanners provide 3D data on today's mobile mapping systems[1]. Future military combat vehicles could benefit from these developments, with the additional focus on precise geolocation, target detection and tracking, and target handoff between vehicles. Such applications require exact knowledge of the geometric constellation of the positioning hardware (POS, the position and orientation subsystem, e.g., GNSS/IMU, odometry) and the LiDAR sensor(s) on the vehicle. Although the attachment of sensors to the mobile sensor carrier can be carefully planned, constructed and adjusted at the time of their installation, various influences can lead to a slow or sudden change in both the placement and orientation of the sensors: unprofessional maintenance or replacement of a device, fatigue of the sensor attachment during its regular use, or the direct impact of force on the vehicle can slightly change the previously identified placement and orientation of the sensor on its carrier. If a LiDAR sensor is affected in this way, the resulting georeferenced point clouds become blurred, as distance measurements are misinterpreted with wrong starting point and direction. To overcome this loss of precision, an extrinsic (re-)calibration of the system is necessary.

1.1 Direct georeferencing of LiDAR range measurements

A typical MLS system consists of several spatially separated parts. These are the LiDAR sensor(s) and the components of the POS, which typically comprises one or more GNSS receivers, a wheel odometry sensor, and the inertial measurement unit (IMU) as its core element. Like a camera, the LiDAR sensor defines its own 3D coordinate frame. On the other hand, the navigation solution provided by the POS refers to a well-defined coordinate frame of the sensor carrier, whose position and orientation in relation to the world coordinate system (e.g., ECEF) is measured. The exact knowledge of the mutual placement and alignment of the sensor's and vehicle's coordinate frames is of great importance for precise data acquisition (see Figure 1).

*marcus.hebel@iosb.fraunhofer.de; phone +49 7243 992-323; fax +49 7243 992-299; www.iosb.fraunhofer.de

Generally, the lever arm d_{LiDAR} of the LiDAR sensor in the vehicle's coordinate frame can be determined with sufficient accuracy once the system is assembled. More effort is necessary to determine the orientation R_{LiDAR}, i.e., the alignment of the LiDAR sensor's coordinate frame relative to that of the vehicle. Typically, the LiDAR sensor makes use of the time-of-flight distance measurement principle, and opto-mechanical scanning provides a specific scan pattern, in which the distance $\rho_L(t)$ measured at time t is directed according to the scanning geometry. Together with the navigational information $p_N(t)$ and $R_N(t)$, the LiDAR measurements are directly georeferenced in the following way:

$$p_L(t) = p_N(t) + R_N(t) \circ \left[R_{LiDAR} \circ r_L(t) + d_{LiDAR} \right] \tag{1}$$

Equation (1) is given with the following notations:

$r_L(t)$:   the 3D point measured by the LiDAR sensor in its own coordinate frame, $\|r_L(t)\| = \rho_L(t)$.

R_{LiDAR}:   3×3 rotation matrix describing the orientation of the LiDAR sensor relative to the vehicle's coordinate frame (boresight direction).

d_{LiDAR}:   vector describing the position of the LiDAR sensor in the vehicle's coordinate frame (lever arm).

$p_N(t)$:   position of the vehicle, i.e., the origin of its coordinate frame, at time t in the world (a Cartesian geographic coordinate system, e.g., ECEF), measured by the POS.

$R_N(t)$:   3×3 rotation matrix that describes the orientation of the vehicle in the world, measured by the POS. In case of an ENU or NED coordinate system, a specific sequence of Euler angles of $R_N(t)$ is *roll*, *pitch*, and *yaw*.

$p_L(t)$:   the geocoordinates of the resulting "*LiDAR point*".

The aggregated points $p_L(t)$ acquired within a time interval $[t_1, t_2]$ are usually called a *LiDAR point cloud* or, more specifically, an *MLS point cloud* in the case of mobile laser scanning.
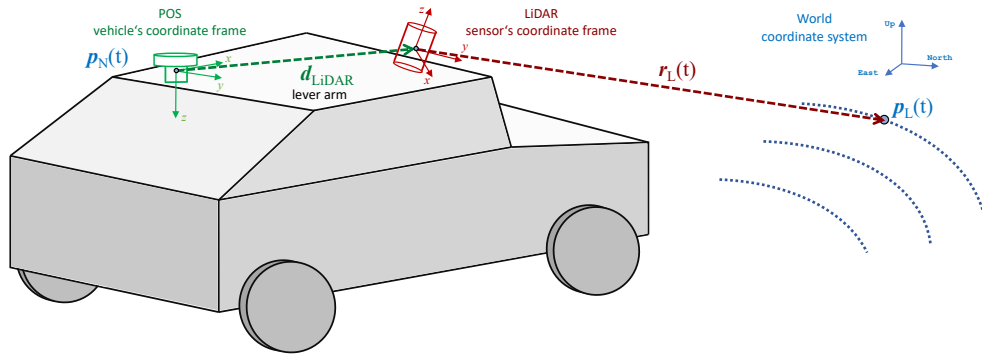

Figure 1. Different coordinate frames (vehicle, sensor, world) and direct georeferencing of LiDAR points.

1.2 Extrinsic calibration of the mobile LiDAR system

Direct georeferencing of laser range measurements provides a data acquisition method that is appropriate for mobile surveying. However, the accuracy of the derived 3D point clouds is influenced by several factors, reflecting the complexity of the MLS system[2][3]. Besides varying exactness of the navigational information sources (GNSS errors, IMU drift), several systematic effects can lead to reduced accuracy of point positioning. Exemplary additional limiting factors are the scanning precision and ranging resolution of the specific LiDAR device. Further negative effects can be introduced by inaccurate synchronization of the system components. As already explained, significant offsets are caused by mounting errors or incorrect lever arms (displacements between LiDAR sensors and the POS subsystem). This paper deals with the automatic correction of these mounting errors, assuming that all other influences were reduced to a minimum. For example, statistical variations in GNSS-based positioning can be reduced by RTK corrections, or simply by considering only short time intervals $[t_1, t_2]$ in which a stable GNSS satellite constellation can be expected, e.g., 20 seconds.

In the context of this paper, *extrinsic calibration* of the mobile LiDAR system means the automatic determination of a correction to Equation (1) with a reorientation R_C and a relocation d_C of the LiDAR sensor in the following way:

$$p_L(t) = p_N(t) + R_N(t) \circ \left[R_{LiDAR} \circ \left(R_C \circ r_L(t) + d_C \right) + d_{LiDAR} \right] \qquad (2)$$

Equation (2) also implies that, after the calibration, the corrected boresight direction of the LiDAR sensor is $R_{LiDAR} \circ R_C$, which means that, in the vehicle's coordinate frame, the original boresight direction R_{LiDAR} is adjusted by the rotation $R_{LiDAR} \circ R_C \circ R^T_{LiDAR}$. The respective corrected lever arm is $d_{LiDAR} + R_{LiDAR} \circ d_C$. As mentioned before, we feel confident that the lever arm can be determined with sufficient accuracy by other means, e.g., by simple measurement with a measuring tape. A boresight error has a much greater impact on the point positioning accuracy. For example, a misalignment of 0.6° results in a displacement of 1.0 m for points at a distance of 100 meters. In this case, a slightly incorrect lever arm is of minor importance, and for this reason we mainly focus on automatic boresight calibration.

After a brief overview of some related work in Section 2, we give a detailed description of the proposed calibration method in Section 3. Section 4 presents the performed experiments and describes their results. Finally, some concluding remarks follow in Section 5.

2. RELATED WORK

Over the last decades, the registration of 3D point clouds, LiDAR-based simultaneous localization and mapping (LiDAR-SLAM), and the calibration of mobile 3D sensor systems have been investigated by many scientists[4][5]. These topics are inherently different, but they are nevertheless interrelated. Considering only the registration of given point clouds ignores the circumstances of data acquisition and tries to optimize the data themselves, e.g., by applying the well-known ICP method. However, ICP can also be the basis for LiDAR-SLAM[6]. LiDAR-SLAM tries to reconstruct the sensor trajectory based on the sensor data, typically presuming a well calibrated sensor system. The calibration of a 3D sensor system aims at optimizing the sensor parameters so that the overall point positioning accuracy is implicitly improved. As in our previous work[7], we address the calibration of mobile LiDAR systems that include a POS subsystem to *measure* the sensor trajectory, and where this trajectory information is used for direct georeferencing.

Different measures of data quality have been proposed to assess the consistency of overlapping point clouds. To name but a few examples: least-squares matching of LiDAR data in a TIN structure[8], attributes derived from DEM differences[9], planimetric accuracy evaluated by comparing automatically extracted ridge lines[10], distances between homologous geometrical features[11], quality of fit between conjugate surface elements[12], or point-to-surface distances in overlapping parts of point clouds[13]. The above examples mainly deal with airborne laser scanning data. However, the methods are most often transferable to vehicle-based LiDAR sensing. Recent work considered mobile mapping systems in general, using a cost function based on several geometric features derived from the local 3D structure tensor[14]. Similarly, we minimize the average scatter of the measured 3D points, assuming a certain occurrence of smooth surfaces in the scene which are scanned multiple times. The overall point scatter is quantified as the average smallest eigenvalue of local principal component analysis (PCA).

In adverse cases, existing 3D point clouds are nonlinearly distorted by calibration errors, but parameters of direct georeferencing have not been stored. Even then there are methods to improve the data quality[16][17]. If, as in our case, laser range measurements and the POS data are available synchronously, these data can be used to determine potential assembly errors with a rigorous approach, e.g., by estimating the system calibration parameters such that 3D points representing a plane are conditioned to show best possible planarity[18]. In the meantime a couple of contributions have been made on the subject of MLS system calibration[19][20], including methodically advanced methods[14][15]. As we do not intend to exceed any existing methodology, this paper is more application-oriented. We present our method, which is applicable to the given task, yet lightweight and easy to implement. With the experiments we demonstrate the applicability to our existing experimental MLS system (see Section 4), and we focus on the analysis of the influence of scene characteristics on the calibration method and its results.

3. PROPOSED CALIBRATION METHOD

As we described in the introduction, the use of an incorrectly configured mobile LiDAR system leads to a blurred 3D point cloud of the scene through which the vehicle has moved (see Figure 2), because the distance measurements $r_L(t)$ are misinterpreted with wrong starting point $p_N(t) + R_N(t) \circ d_{LiDAR}$ and direction $R_N(t) \circ R_{LiDAR}$. With Equation (2), a reorientation R_C and a relocation d_C of the LiDAR sensor are to correct the misalignment and displacement of the sensor.
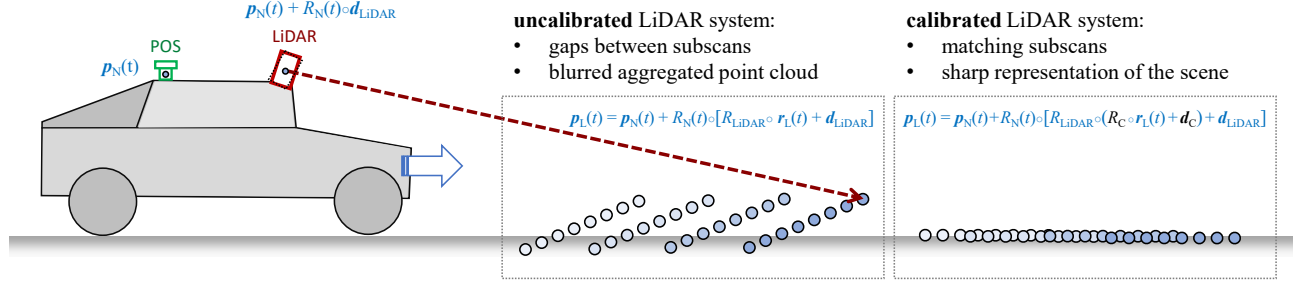
Figure 2. Data acquisition with the uncalibrated LiDAR system results in a blurred aggregated point cloud, while the point cloud acquired after extrinsic calibration is a sharp 3D representation of the scene.

3.1 Motivation of the approach

The situation of blurred 3D point clouds is comparable to unsharp images taken with an unfocused SLR camera. With a lens to be manually focused, the photographer looks through the camera's viewfinder and rotates the focus ring back and forth until the appropriate focus setting is achieved, i.e., until the image appears sharp. In principle, the same happens with the contrast-detection autofocus of modern digital cameras. Here, the average contrast between adjacent pixels of the sensor array is measured, while the optical system is adjusted automatically until the maximum contrast is obtained.

In 2D imaging only one parameter needs to be adjusted to get a sharp image, namely the focus setting of the lens. If we transfer this procedure to the calibration of the MLS sensor system, which is a 3D imaging system moving through the scene, a total of six parameters must be tuned, namely the three Euler angles of R_C (boresight correction) and the three coordinates of d_C (correction to the lever arm). What is needed for an automatic evaluation is a measure that distinguishes a good setting of the six parameters from a bad one.

3.2 Measuring the quality of the acquired MLS point clouds

In our approach, we assess and optimize the quality of the acquired MLS point clouds by quantifying and minimizing the average local scatter of the 3D points. This assumes that the scene is characterized by many smooth surfaces, and that a calibrated MLS system repeatedly measures 3D points representing these smooth surfaces (like the ground level in Figure 2). A proportionate occurrence of inhomogeneous structures, e.g., vegetation, leads to an almost constant background noise, since the scanning of these structures under no assumed sensor pose produces smooth surfaces.

Let P denote the set or a subset of directly georeferenced 3D points acquired within the time interval $[t_1, t_2]$ by the MLS system under consideration. First, a k-d tree data structure is built to enable nearest neighbor searching in P. Let $p_i \in P$ be an arbitrary element of P. Furthermore, let $\{p_{ij}\}_{j=1,...,N}$ be the set of N nearest neighbors of p_i, where N is a predefined integer number that is kept fixed during the analysis. We decided to consider a fixed number of neighboring points instead of a fixed neighborhood radius in order to better adapt the method to varying local point densities. With $p_{i0} := p_i$, the centroid $\bar{p}_i$ of the local point neighborhood is defined as:

$$\bar{p}_i = \frac{1}{N+1} \sum_{j=0}^{N} p_{ij} \tag{3}$$

With these notations and definitions, the covariance matrix C_i of p_i is given as follows:

$$C_i = (p_{i0} - \bar{p}_i, \ldots, p_{iN} - \bar{p}_i) \circ (p_{i0} - \bar{p}_i, \ldots, p_{iN} - \bar{p}_i)^T \tag{4}$$

The 3×3 covariance matrix defined in Equation (4) is symmetrical and positive semi-definite, hence the eigenvalues λ_{i1}, λ_{i2}, and λ_{i3} of C_i are non-negative real numbers. The corresponding eigenvectors v_{i1}, v_{i2}, and v_{i3} of C_i are the principal axes of the local point neighborhood $P_i = \{p_{ij}\}_{j=0,...,N}$. Each eigenvalue λ_{ik}, divided by the number $N+1$ of points in P_i, is a normalized measure of the point scatter in the direction of v_{ik}. The result of this principal component analysis (PCA) can be illustrated as an ellipsoid, in which the principal axes are the three orthogonal vectors $\lambda_{i1}v_{i1}$, $\lambda_{i2}v_{i2}$, and $\lambda_{i3}v_{i3}$, see Figure 3 (a). By convention, the indices k are chosen such that $\lambda_{i1} \leq \lambda_{i2} \leq \lambda_{i3}$. If only λ_{i1} is close to zero, this indicates a locally planar surface, with v_{i1} as an approximation of its local normal direction n_i, see Figure 3 (b). Let n_P be the number of points in P. Our measure S for the average quality of fit to be optimized by the calibration procedure is:

$$S = \frac{1}{n_P \cdot (N+1)} \sum_{i=1}^{n_P} \lambda_{i1} \tag{5}$$

Equation (5) means that the local principal component analysis is performed for every local point neighborhood P_i in P, and that the mean value of all smallest eigenvalues, normalized with respect to the number of points in each local point neighborhood, indicates the overall quality of the point cloud P. Lower values of S indicate higher quality.
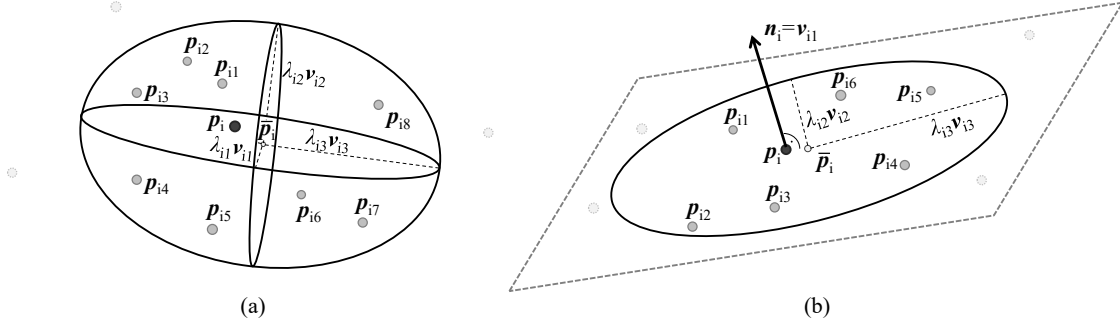

Figure 3. (a) Ellipsoid illustrating the principal axes of a local point neighborhood P_i. (b) In case of a smooth (locally planar) surface, the smallest eigenvalue is close to zero and the corresponding eigenvector approximates the normal direction.

3.3 Maximizing the quality of the acquired MLS point clouds

With the calibration guideline formulated in Equation (2) and the quality indicator of Equation (5), the calibration can be performed by maximizing the overall point cloud quality, i.e., by minimizing S. The reorientation R_C and the relocation d_C of the LiDAR sensor give a set of six parameters influencing S. We decompose the rotation R_C into rotations of Euler angles (α, β, γ) about the axes of the sensor's coordinate system, and we denote the components of d_C by $d_C=(u, v, w)$. If the angles α, β, and γ are small (e.g., $\alpha, \beta, \gamma < 3°$, α, β, γ in radians), a good approximation of R_C is

$$R_C \approx \begin{pmatrix} 1 & -\gamma & \beta \\ \gamma & 1 & -\alpha \\ -\beta & \alpha & 1 \end{pmatrix} \quad \text{for small angles } \alpha, \beta, \gamma \text{ in radians } (\alpha, \beta, \gamma < 0.06). \tag{6}$$

Nevertheless, we use the correct calculation of the rotation $R_C = R_x(\alpha) \circ R_y(\beta) \circ R_z(\gamma)$ with partial rotations in the given order. Every 6-tuple $(\alpha, \beta, \gamma, u, v, w)$ describes a configuration of the MLS system, and considering this configuration in direct georeferencing yields a point cloud $P_{(\alpha, \beta, \gamma, u, v, w)}$ for which its quality is indicated by $S(\alpha, \beta, \gamma, u, v, w)$. Different numerical approaches are feasible to find the optimal setting, which is

$$(\alpha, \beta, \gamma, u, v, w)_{\text{opt}} = \arg\min S(\alpha, \beta, \gamma, u, v, w) \tag{7}$$

The most straightforward numerical approach to find the optimum is the brute-force search or exhaustive search, in which all possible combinations $(\alpha, \beta, \gamma, u, v, w)$ are tested. Since the 6D parameter space is continuous, it must be discretized to implement the exhaustive search, which thereby becomes a *full grid search*, see Figure 4 (a). Obviously, the main disadvantage of the full grid search is the number of candidates to be examined, which usually is unacceptably large. For example, if we consider the grid generated by sampling the angular values between -3° and +3° in steps of 0.1°, and the position values between -1 m and +1 m in steps of 5 cm, this would result in $61^3 \cdot 41^3$ combinations, hence more than 10^{10} configurations to be tested. We follow different strategies to explore and reduce the search space:

- We separate the determination of the optimal boresight direction $(\alpha, \beta, \gamma)_{\text{opt}}$ from the determination of the optimal lever arm $(u, v, w)_{\text{opt}}$. This is motivated by the assumption that, as mentioned before, the lever arm can be better measured by other means than data-driven. If that is the case and we focus on the boresight alignment, the search space in the above sampling example is reduced to $61^3 \approx 230,000$ elements.

- Instead of a full grid search, we usually perform a *recurrent dimensional search*. This means only one parameter is varied at a time to find a minimum of S in that dimension, while the others are kept fixed. For example, we start with $(-3° \leq \alpha \leq +3°, 0, 0)$, continue with $(\alpha_{\text{opt}}, -3° \leq \beta \leq +3°, 0)$ and then $(\alpha_{\text{opt}}, \beta_{\text{opt}}, -3° \leq \gamma \leq +3°)$. We repeat this dimensional search for several runs, each time with the previous $(\alpha_{\text{opt}}, \beta_{\text{opt}}, \gamma_{\text{opt}})$ in its center, see Figure 4 (b).
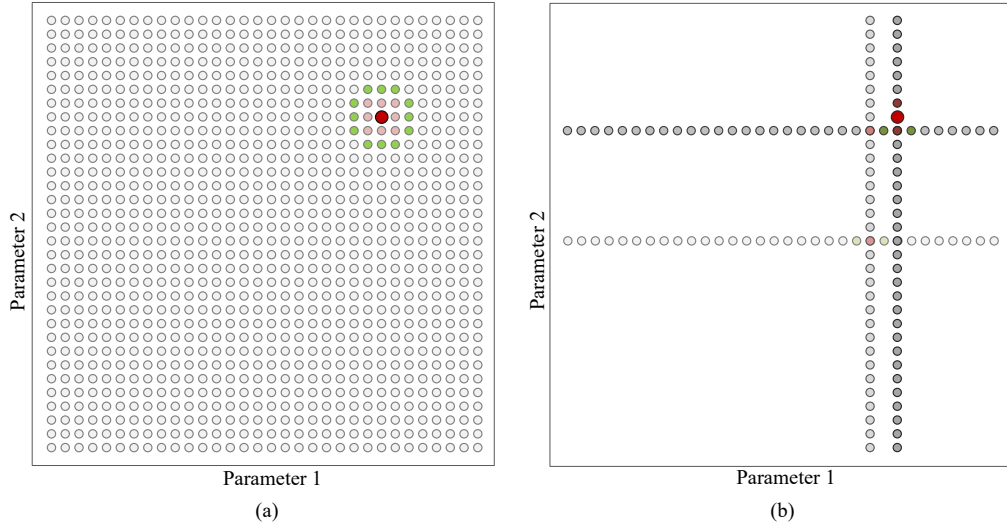
Figure 4. (a) Full grid search in a two-dimensional parameter space, (b) recurrent dimensional search.

The recurrent dimensional search can be complemented by refining the step-size, i.e., by decreasing the sampling distance for the parameter space in each iteration. Recurrent dimensional search can, but need not find the global optimum. This depends on the specific nature of the function represented by $S(\alpha, \beta, \gamma, u, v, w)$ or $S(\alpha, \beta, \gamma)$, e.g., its continuity and convexity. In the experiments, we analyzed the appearance of this function by actually performing the full grid search for $S(\alpha, \beta, \gamma)$ to get an impression of the feasibility of this approach under different conditions.

4. EXPERIMENTS

4.1 Experimental platform

At Fraunhofer IOSB, the experimental multi-sensor vehicle "MODISSA" (Mobile Distributed Situation Awareness) is used for experiments in the context of automotive safety, security, and military applications[21]. It is currently equipped with four LiDAR sensors: two Velodyne HDL-64E sensors above the windshield and two Velodyne VLP-16 sensors above the rear window. Additionally, eight CCD-cameras are mounted on the roof edges. The cameras are not relevant for this paper, they are only mentioned for completeness. This arrangement of sensors allows the coverage of the environment around the vehicle, both with LiDAR sensors and with video cameras. Furthermore, a pan-tilt-head with an IR-camera and a video camera is placed directly behind the two Velodyne HDL-64E sensors. In the context of military motivated research work, it can also be used to simulate effectors. Figure 5 (left) shows the vehicle and its sensor arrangement. The central clock of MODISSA is provided by an Applanix POS LV 520 consisting of two GNSS receivers, an odometry sensor, and an IMU. The POS allows direct georeferencing of the LiDAR data.

Figure 5: IOSB's sensor vehicle MODISSA (left), and detail view of the two Velodyne HDL-64E laser scanners (right).

We used only the two Velodyne HDL-64E sensors of MODISSA for the experiments, but the two Velodyne VLP-16 can be treated in the same way. Each Velodyne HDL-64E is configured to have a rotational frequency of 10 Hz and acquires 130,000 range measurements (3D points) per rotation with distances up to 120 m. Each sensor has four laser emitter groups of 16 single lasers, and two detector groups of 32 single detectors. Thus, each sensor consists of 64 emitter-detector pairs (i.e., 64 laser rangefinders), which divide the vertical field of view of 26.8° into 64 scan lines. To avoid direct illumination of the detectors of one sensor by laser pulses of the other one, we placed a black panel between the two sensors, as can be seen in Figure 5 (right). Remaining crosstalk effects are eliminated by data filtering[22].

The geometrical constellation of the laser scanners is adaptable to the respective task. For example, the detection of pedestrians[23] requires an upright axis of the laser scanner to ensure 360° situational awareness. In contrast, monitoring of the airspace[24] or mobile mapping of urban areas[25] can benefit from an inclined axis of rotation, which enables the acquisition of data points on the facades of buildings even at greater heights. We use wedges with different inclinations and orientations that can be placed under the sensors, cf. Figure 5 (right). Each time the geometrical constellation of the laser scanners is changed in relation to the POS, the multi-LiDAR sensor system needs to be calibrated.

Figure 5 depicts the configuration that was kept unchanged during the experiments in the scope of this paper. The Velodyne HDL-64E laser scanner above the driver's seat, which we refer to as V2, had an upright position, while the other, V1, was positioned on a wedge at a 25-degree angle to the horizontal, rotated backwards and inwards at a 45-degree angle. The Applanix POS LV 520 was configured such that the coordinate frame of the vehicle has its origin below that wedge under V1, with its x-axis pointing in driving direction, y to the right and z to the ground. The boresight directions R_{LiDAR} of V1 and V2 had been thoroughly pre-calibrated beforehand, using the same methods as described in this paper. Their lever arms d_{LiDAR} were specified by the construction plans of the sensor carrier.

4.2 Layout of the experiments

One focus of this paper is on quantifying the influence of driving maneuvers and, particularly, scene characteristics on the calibration method and its results. On October 1st 2019, we used the sensor car MODISSA to acquire mobile laser scanning data in and near the city of Ettlingen, Germany (N 48.947°, E 8.411°). In this run, one hour of data acquisition resulted in more than 35,000 single scans (360° rotations of the scanner head) of each of the two Velodyne HDL-64E laser scanners. After georeferencing of the laser range measurements, this corresponds to more than 6 billion 3D points in total. We have selected five segments of this measurement run with different properties of the scenarios and tested the calibration procedure on data recorded within these zones. Their approximate locations are shown in Figure 6.
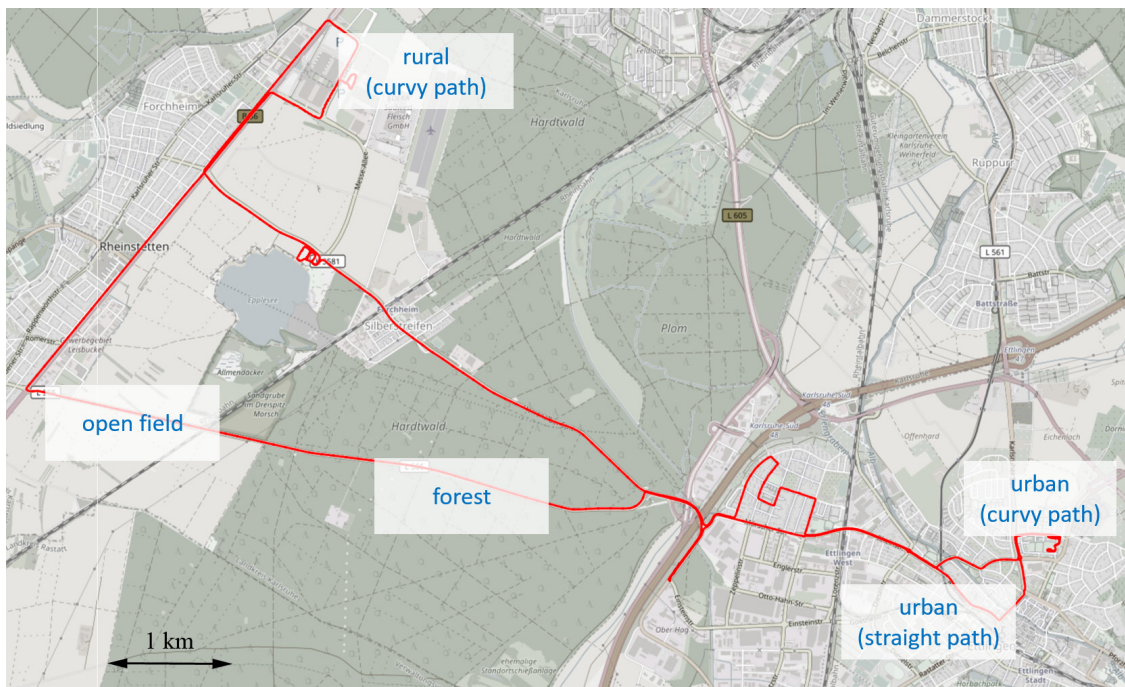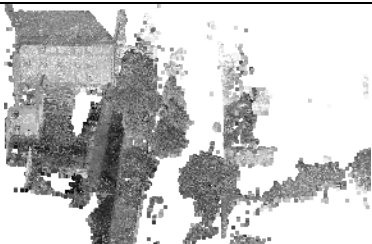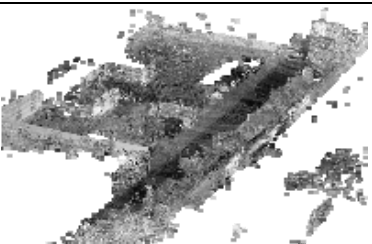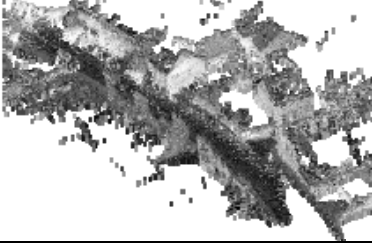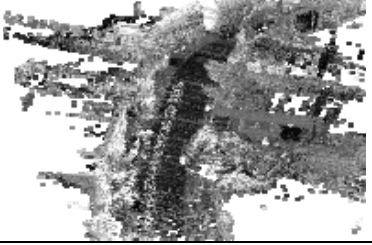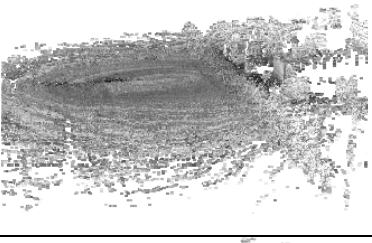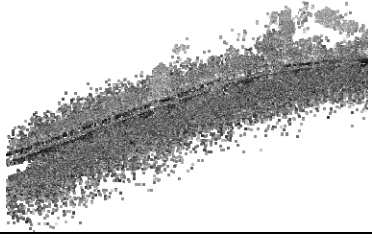

Figure 6. Track covered in the measurement run (red) and different test zones (text boxes). Map source: OpenStreetMap.

The vehicle can be driven in paved or unpaved terrain at different speeds, in a straight line or with curvy driving maneuvers, e.g., zigzag. The latter has the advantage of a greater variety of angles at which the scene is captured. In the case of our experimental system, however, such maneuvers are not feasible in places where MODISSA participates in general road traffic. Speed limits and other traffic regulations must be observed. Wherever it was possible at all, curvy driving maneuvers were performed rather slowly, while the route otherwise followed the course of the road at an adapted speed.

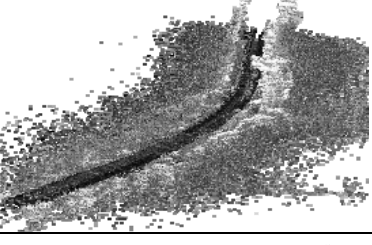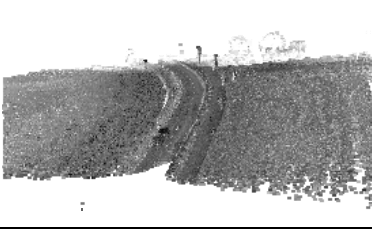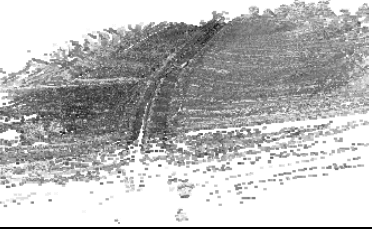Table 1 shows an exemplary view for each of the five scenarios together with visualized sections of the directly georeferenced point clouds captured by the Velodyne HDL-64E laser scanners V1 and V2. Each point cloud shown consists of the measurement data acquired within 10 seconds. The gray values of the points in the point clouds correspond to the intensity of the respective pulse echo, measured by the laser scanners themselves. The views in the direction of travel have been captured by selected cameras on the vehicle, whose image data were recorded synchronously.

Table 1. Detailed views of the five selected scenarios. Camera images and visualization of the georeferenced point clouds.

scenario	camera image	laser scanner V1	laser scanner V2
1. urban (curvy path, zigzag)			
2. urban (straight path)			
3. rural (curvy path)			
4. forest (straight path)			
5. open field (straight path)			

4.3 Data preparation and preprocessing

As described in Subsection 4.2, we recorded all raw data of the measurement run, including the range measurements of the two laser scanners V1 and V2 as well as the POS data. With regard to the notations defined by Equation (1), we thus have all $p_N(t)$, $R_N(t)$, and $r_L(t)$. The boresight direction R_{LiDAR} of each of the two laser scanners had been carefully pre-calibrated, and the lever arms d_{LiDAR} are known from construction plans of the sensor platform. Therefore, we can reasonably assume that the configuration, i.e., the geometric constellation of all components in this MLS system is known with sufficient accuracy. When considering Equation (2), this means that no corrections would be necessary, i.e., in that case R_C is the identity matrix and d_C is the zero vector.

In order to test the proposed calibration method, we intentionally set two incorrect boresight directions $R_{V1,A}$ and $R_{V1,B}$ for laser scanner V1, and similarly $R_{V2,A}$ and $R_{V2,B}$ for laser scanner V2. The two variants A and B of the incorrect boresight direction were achieved by manipulating the respective correct R_{LiDAR} in such a way that, in case of variant A, its correction R_C would be given by the angles $(\alpha, \beta, \gamma)_A = (+2.3°, +0.7°, -1.3°)$, and in the case of variant B by the angles $(\alpha, \beta, \gamma)_B = (+0.8°, -2.1°, -1.4°)$. In short: we intentionally based the direct georeferencing of 3D points on false boresight directions of the laser scanners, but we know the amount of misalignment introduced into the MLS system that way, i.e., we know the ground-truth for the calibration method. Figure 7 exemplarily shows the impact of using an incorrect boresight direction of only a few tenths of a degree. Regarding the lever arms d_{LiDAR}, we kept the known setting because, as mentioned above, we focus on the boresight alignment.

By replacing R_{LiDAR} in Equation (2) by $R_{V1,A}$, $R_{V1,B}$, $R_{V2,A}$, or $R_{V2,B}$, we georeferenced the range measurements to obtain 3D point clouds for the five different scenarios. Hence, we have twenty different examples for the calibration procedure. The respective time intervals $[t_1, t_2]$ were chosen to cover 15 seconds, but the calibration method was also tested on subsets of the point clouds corresponding to 10 seconds or 5 seconds of measurement time. The preprocessing of the point clouds includes temporal filtering of erroneous points caused by crosstalk in the multi-LiDAR sensor system[22]. Additionally, we homogenize the point density in the scene by the following filter: a point is removed from the point cloud if $0.0125 \cdot \|r_L(t)\| < rand$, where *rand* is a random (floating point) number between 0 and 1 that is generated for each point. Besides homogenizing the overall point density and therefore the impact of near and far points, this filter reduces the amount of data enormously and thus improves the processing time.

(a) (b) (c)
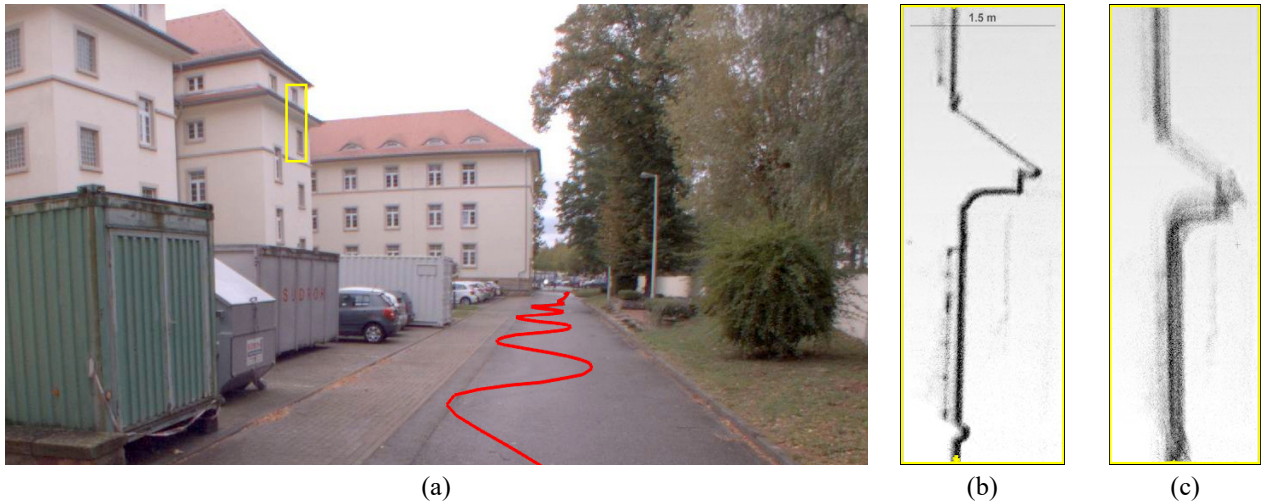
Figure 7. (a) View of scenario "urban (curvy path)" with visualized path (red) and section (yellow) of the 3D point cloud obtained by: (b) direct georeferencing using the correct R_{LiDAR}, and (c) with slightly incorrect boresight direction R_{V1}.

4.4 Results

The calibration method uses only a few parameters to control its operation. The main parameter is the number N of neighboring points that form the local point neighborhood for which the principal component analysis is performed. An additional setting is the length of the time interval $[t_1, t_2]$ in which data for the calibration method are collected. In our case, we vary the number of consecutive 360° scans of the Velodyne laser scanners, each of these scans corresponding to a time interval of 0.1 seconds.

In the first part of the experiments, we applied the calibration method for the boresight alignment with a recurrent dimensional search to the data of sensors V1 and V2, whose georeferencing was based on the variants A and B of incorrect boresight directions. We tested the settings 50, 100 and 150 for the number N of neighboring points, and we varied the considered time interval between 5, 10 and 15 seconds for each of the five scenarios. The search interval for the angles (α, β, γ) of the boresight correction R_C was set to [-3°, +3°] with an 0.1° increment, and three iterations of the recurrent dimensional search were performed. The lever arms of V1 and V2 remained untouched at their known coordinates.

All results of the boresight alignment after applying the calibration method with recurrent dimensional search are shown in the diagrams in Table 2. As already mentioned, the ground-truth for the correction R_C of variant A is represented by the angles $(\alpha, \beta, \gamma)_A = (+2.3°, +0.7°, -1.3°)$, and in case of variant B by the angles $(\alpha, \beta, \gamma)_B = (+0.8°, -2.1°, -1.4°)$. These nominal values are shown in the diagrams by dotted lines. In total, Table 2 lists the results of 3 (N = 50, 100, 150) · 3 ($[t_1, t_2] \triangleq 5$, 10, 15 seconds) · 2 (laser scanners V1 and V2) · 2 (variants A and B) · 5 (number of scenarios) = 180 calibration runs. The results are discussed in Subsection 4.5.

In the second and main part of the experiments, we actually performed the full grid search for the angles (α, β, γ) for both sensors V1 and V2, starting from both variants A and B of incorrect boresight directions. Within these experiments, we fixed the number N of neighboring points at N=100 and set the considered time interval of data acquisition for the calibration method to 10 seconds. Since we did not intend to correct the lever arms, the parameter space for the full grid search was three-dimensional, namely the three angular dimensions α, β, and γ. Again, the search interval for the angles (α, β, γ) of the boresight correction R_C was set to [-3°, +3°] with a step size of 0.1°. The full grid search was applied for 2 (laser scanners V1 and V2) · 2 (variants A and B) · 5 (number of scenarios) = 20 calibration runs, each run consisting of $61^3 = 226{,}981$ calculations of $S(\alpha, \beta, \gamma)$.

All results are shown in the diagrams in Table 3. For a better understanding of these diagrams, two examples are shown in Figure 8 in a larger format. The nominal values $(\alpha, \beta, \gamma)_A$ or $(\alpha, \beta, \gamma)_B$, respectively, are marked by a black cross in the 3D parameter space. Ideally, the result of the calibration run should be exactly these three angles defining R_C. The dots in the colors from green to red represent the 0.05 quantile of $S(\alpha, \beta, \gamma)$ in the parameter space, i.e., the 5% of the angles that give the best boresight corrections. The color representation is analogous to the illustration in Figure 4 (a). In addition, the blue cross shows the position of the found minimum of $S(\alpha, \beta, \gamma)$, i.e., the actual result of the calibration run. Whether the calibration was successful can be assessed by the distance between the blue and the black cross. The shape of the parameter set of the 0.05 quantile provides information on how well the minimum of $S(\alpha, \beta, \gamma)$ can be localized. For example, the 0.05 quantile in Figure 8 (a) has an almost spherical shape, which indicates that the uncertainty of the boresight correction angles is approximately the same in all angular dimensions. The situation is a bit different in the example shown in Figure 8 (b), where the position of the minimum of $S(\alpha, \beta, \gamma)$ is still close to the nominal coordinates $(\alpha, \beta, \gamma)_B$, but the precision of this position is lower in one direction. The evaluation that can be made based on these diagrams is (1.) the calibration procedure worked most reliably if the 0.05 quantile has a clearly defined, almost spherical shape, and (2.) the result is better the closer the blue cross is to the black cross.

(a): $S(\alpha, \beta, \gamma)$ for sensor V1, variant A,
scenario: urban (curvy path, zigzag)

(b): $S(\alpha, \beta, \gamma)$ for sensor V1, variant B,
scenario: rural (curvy path)
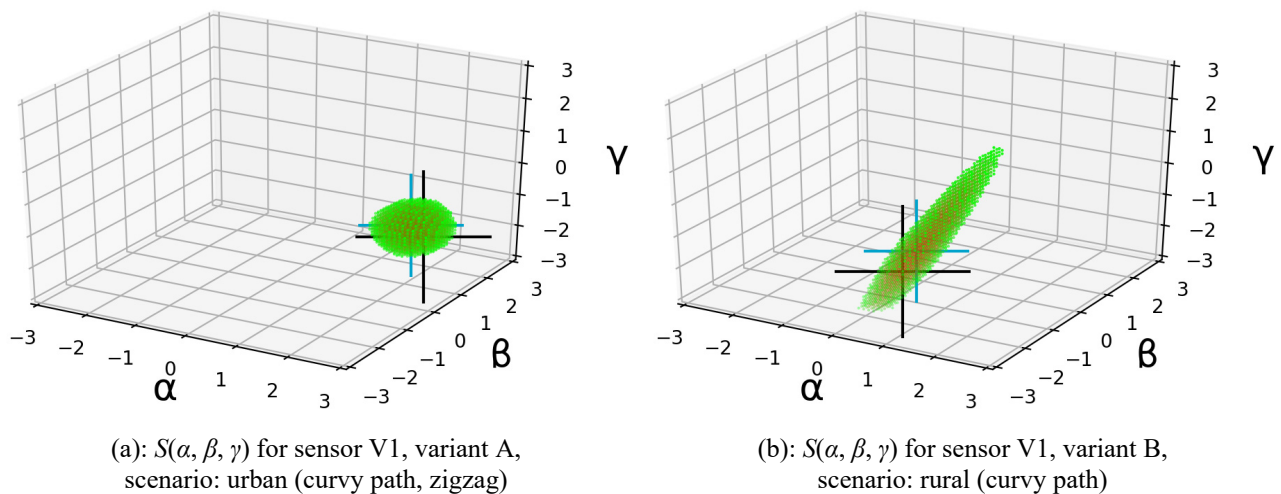
Figure 8. Two exemplary diagrams for the results of the full grid search for R_C to correct (a) $R_{V1,A}$ or (b) $R_{V1,B}$.

Table 2. Calibration results for the laser scanners V1 and V2 with variants A and B of incorrect boresight directions, using variations of **recurrent dimensional search** with different settings. The color coding for the Euler angles is α, β, γ.

scenario	boresight error variant A	boresight error variant B
1. urban (curvy path, zigzag)		
2. urban (straight path)		
3. rural (curvy path)		
4. forest (straight path)		
5. open field (straight path)		

Table 3. Results for sensors V1 and V2, variants A and B, using **full grid search** with N=100 and $[t_1, t_2] \triangleq 10$ seconds. Each diagram shows the 0.05 quantile of $S(\alpha, \beta, \gamma)$, i.e., the 5% best performing boresight correction angles in parameter space.

| sc.	sensor V1, variant A	sensor V1, variant B	sensor V2, variant A	sensor V2, variant B
1				
2				
3				
4				
5				
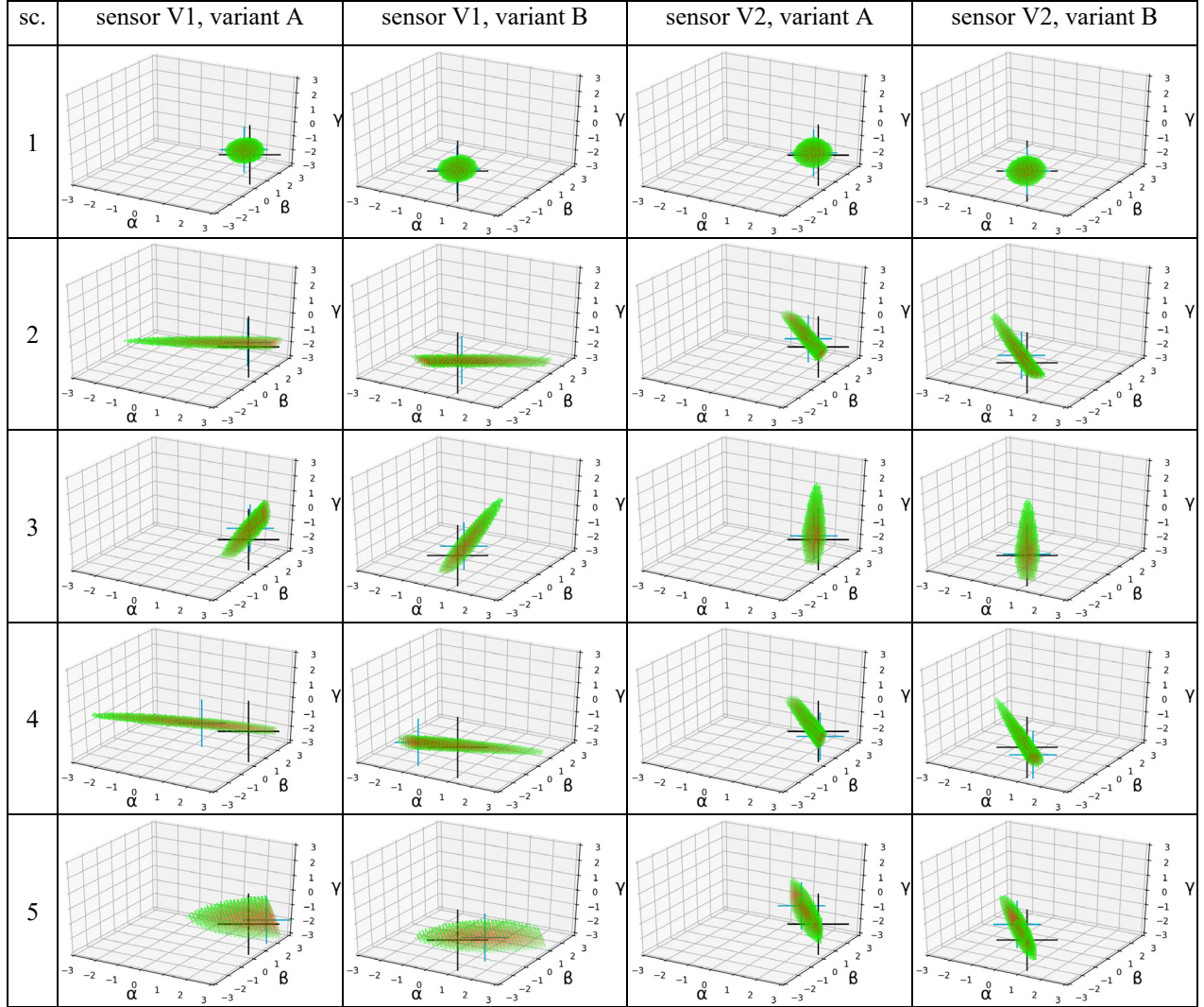
In the third and last part of the experiments, we finally performed the full grid search for the coordinates (u, v, w) of d_C, which represent a correction to the lever arm d_{LiDAR} in the coordinate system of the LiDAR sensor, cf. Equation (2). Although our main focus in this paper is on boresight corrections, we still wanted to evaluate the procedural capability for corrections of the lever arms. In this last part of the experiments, the boresight directions of V1 and V2 were held at their known setting R_{LiDAR}, and we considered only the components (u, v, w) of d_C to be calibrated. Since we started from the known lever arms as well, the nominal value of d_C in both cases is the zero vector, which means that the output of the calibration procedure should ideally be $(u, v, w)_{opt} = (0, 0, 0)$.

Since this experiment was intended as an add-on, we have only considered the scenario "urban (curvy path)", which turned out to be the most applicable so far. Again, the parameter space for the full grid search was three-dimensional, but now with the three components u, v, and w of d_C. The search interval was set to [-1.5 m, +1.5 m] with a step size of 5 cm. Therefore, the full grid search was applied for two calibration runs (laser scanners V1 and V2), each run consisting of $61^3 = 226,981$ calculations of $S(u, v, w)$. Table 4 shows the two diagrams, in which again the 5% best performing parameters are shown, i.e., the 0.05 quantile of $S(u, v, w)$, together with a black and a blue cross indicating the nominal values and the found values for the correction d_C, respectively. The position of the minimum is $(u, v, w) = (-0.50, 0.10, -1.20)$ in the case of laser scanner V1, and $(u, v, w) = (0.00, 0.00, 0.15)$ in the case of laser scanner V2, indicated by the blue cross.

Table 4. Results for corrections to the lever arms of sensors V1 and V2, using **full grid search** with N=100 and $[t_1, t_2] \triangleq 10$ seconds. The diagrams show the 0.05 quantile of $S(u, v, w)$, i.e., the 5% best performing d_C.

sc.	sensor V1	sensor V2
1		
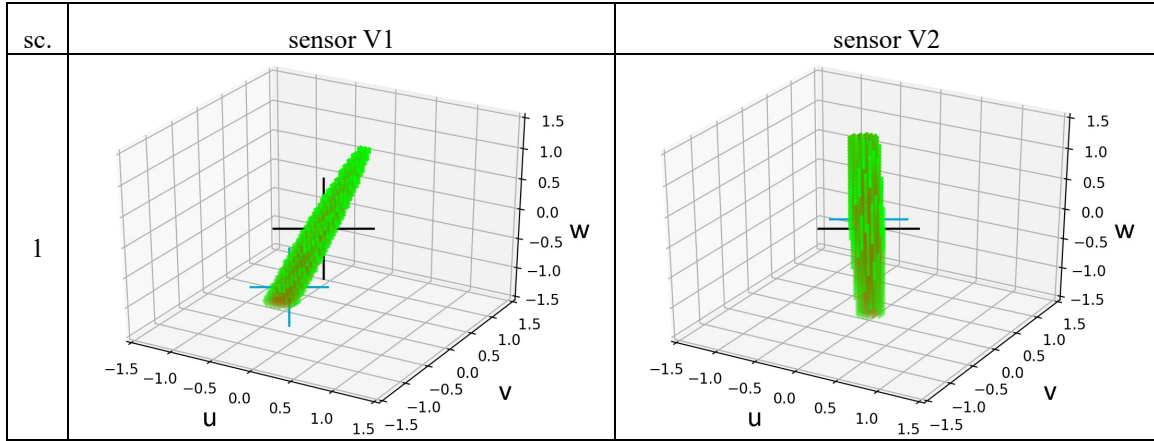
4.5 Discussion of the results

If we first look at the obtained calibration results of the **recurrent dimensional search** of the boresight directions in **Table 2**, we notice significant differences depending on the scene. Even within the tests of a particular scenario, the different settings (N: number of points per local point neighborhood, $[t_1, t_2]$: length of the time interval, i.e. the extent of the point set) are more or less strongly noticeable in the results.

- The scenario "1. urban (curvy path)" scores best by far, also with regard to the stability of the resulting values for different processing parameters. The results are close to the nominal values. Only the runs with a short data acquisition time of 5 seconds are slightly poorer in the case of laser scanner V1, which can also be ascribed to the randomly present scene contents (e.g. buildings mainly on one side of the vehicle, see Figure 7). A longer data acquisition time leads to a better statistical distribution of the orientations of scanned surfaces while driving. However, if the data acquisition time is too long, fluctuations in the vehicle positions p_N measured by GNSS will most likely become noticeable (e.g. due to multipath effects), and the data volume will become too large for processing. Obviously, the most promising driving segments and driving styles are those in urban areas that generate as many variations of the viewing angles as possible within a short time.

- This is also confirmed by the scenario "3. rural (curvy path)", which delivers very good results in the case of the upright laser scanner V2, but only partially in the case of the inclined laser scanner V1. This may also be caused by the accidental presence or absence of scene content. Within this scenario, there was only a sparse building density, so that in comparison to the scenario "1. urban (curvy path)", there was a higher chance of measuring a gap in the respective direction and thus little varying surface orientations.

- The results in the case of the scenario "2. urban (straight path)" are poor, as are those of the scenarios "4. forest (straight path)" and "5. open field (straight path)". While it was to be expected in the case of the latter two, it is quite astonishing in the case of an urban area, where sufficiently many smooth surfaces are usually found even at higher altitudes. Obviously, the curvy driving style with variations of the viewing angles is the most important and, in any case, clearly preferable, which is also shown by the comparatively good performance of the scenario "3. rural (curvy path)".

- Apparently, even under the best conditions, the final result of the calibration can still be expected to vary in the order of 0.1°, which corresponds to a point positioning accuracy of 17 cm at a distance of 100 m.

A question to be answered in this paper is that of the basic suitability of the recurrent dimensional search as a calibration method. With the proposed numerical approach, only this search strategy has the potential of a timely operational usability (several minutes runtime), since the full grid search requires orders of magnitude more computing time (several hours runtime). The recurrent dimensional search requires the function $S(\alpha, \beta, \gamma)$ to have a suitable appearance (such as continuity, convexity), so that an iterated search of the component-wise minimum of the function values converges to the

global minimum. In order for this to happen in a few iterations, a distinct and uniform occurrence of the minimum in all dimensional directions is required, which can ideally be seen in a spherical shape when visualizing the 0.x quantile of $S(\alpha, \beta, \gamma)$. To assess this in more detail, the **full grid search** for the boresight correction angles α, β, and γ was actually carried out as the main analysis within this paper, although the full grid search cannot be used for short-term calibration in practice.

- By visualizing the 0.05 quantile of $S(\alpha, \beta, \gamma)$ in **Table 3**, the full grid search shows why the scenario "1. urban (curvy path)" gives the best calibration results. The almost spherical shape indicates that the recurrent dimensional minimum search can also yield the same result after a few iterations. The respective minimum is close to the nominal values. It should be noted that these nominal values are the result of intentional manipulation of a previously found calibration result, so they can themselves deviate slightly from reality.

- In its visualization, the 0.05 quantile of $S(\alpha, \beta, \gamma)$ of the scenario "3. rural (curvy path)" has at least the shape of an ellipsoid of moderate extensions, which explains why this type of scene can also be considered suitable for calibration. In contrast, the 0.05 quantile of $S(\alpha, \beta, \gamma)$, resulting from scenario "5. open field (straight path)", shows several isolated parts in the case of sensor V2. It is therefore not convex in its overall shape, which is why an iterative procedure is likely to end in a local minimum. Furthermore, the position of the global minimum differs strongly from the nominal values. In general, it can be seen in the scenarios "2. urban (straight path)", "4. forest (straight path)" and "5. open field (straight path)" that the minimum of the function $S(\alpha, \beta, \gamma)$ is difficult to locate in at least one direction in the parameter space.

- The "parameter direction of the highest uncertainty", which can be seen from the stretching of the 0.05 quantile of $S(\alpha, \beta, \gamma)$ in the diagrams of Table 3, cannot be interpreted directly. It refers to α, β, and γ as correction angles, which are given in the coordinate system of the laser scanner, which in the case of V1 is inclined itself (see Figure 5). However, it is easy to imagine laser scanner misalignments in which a single planar surface occurring in the scene is still captured as a plane, e.g., if an upright laser scanner is only rotated in its heading direction and captures the ground plane (like in scenario "5. open field"). In such a case, the characteristics of the scene do not permit calibration, since the calibration procedure lacks suitable structures whose representation in the data varies in quality in the event of varying sensor misalignment.

The results of the third part of the experiments, namely the **tests for automatic correction of the lever arms** of V1 and V2 using data of the scenario "1. urban (curvy path)", can be interpreted in a similar way to the latter. **Table 4** shows the corresponding diagrams. In the case of V1, the found lever arm deviates from its actual position by more than one meter. We had expected from the beginning that lever arms could be measured much better, easier and faster with independent methods. This is confirmed by this result, as even with a simple measuring tape there would be no error of one meter. The coordinates (u, v, w) of the correction to the lever arm can be understood more easily in the case of laser scanner V2, because V2 stands upright and thus the orientation of its coordinate system matches that of the vehicle. It can be seen on the right in the diagram in Table 4 that the 0.05 quantile of $S(u, v, w)$ extends strongly in the height direction w. This means that practically any height correction of the laser scanner's mounting position provides point clouds of equal quality. This is understandable, since during data acquisition in the experiments, the vehicle was moving on a plane (at ground level). Then, changing the lever arm of the laser scanner in height only shifts all data in this direction, but does not change their internal quality. In order to be able to make better automatic corrections of the lever arms with the proposed method, the driving maneuver would not only have to be curvy, it would also have to involve crossing hills (e.g., bumps).

5. CONCLUSIONS

We have presented a method by which misalignments and displacements of LiDAR sensors attached to vehicles can be determined during their operation, i.e., a method by which the extrinsic self-calibration of an MLS system can be performed. Special attention was paid to the broad feasibility and simplicity of the procedure, which makes it also practicable for operational vehicles in the field. The procedure is therefore less focused on data acquisition vehicles in surveying and more on the operational use of vehicle-based LiDAR sensors, even on military vehicles.

The presented method quantifies the quality of the acquired 3D point clouds as a function of parameters describing the geometric constellation of the sensor system on the vehicle. A numerical searching technique is proposed to determine the optimal parameters that maximize the quality of the acquired point clouds. The method of recurrent dimensional search, which is preferred for reasons of runtime, can only work successfully if the quality measure has a simple func-

tional dependency on the parameters. In this paper, this dependency was investigated numerically by performing a full grid search. The authors would like to thank Hennadiy Yatskov, who during his time as a student assistant at Fraunhofer IOSB contributed significantly to the efficient programming of these methods.

As a result, the following can be stated: For an extrinsic calibration in the proposed manner, curvy driving maneuvers (e.g. zigzag) should be performed in a terrain with enough surfaces with varying orientations. An urban area seems to be the most suitable. If this is not available, a zigzag drive between sheds, camp tents, parked vehicles, etc., can still lead to a proper calibration. The determination of the orientation angles of the LiDAR sensor succeeds with an estimated residual error of 0.1°, which corresponds to a point deviation of 17 cm at a distance of 100 m. An independent measuring method is recommended for determining the lever arm of the LiDAR sensor, in the simplest way using a measuring tape. If the lever arm is also to be determined automatically from the LiDAR data, the driving maneuver must include vertical variations, for example by driving over bumps.

Our method allows us to combine the measurement data of several LiDAR sensors that are used on the same vehicle in order to eliminate any offset between the 3D measurement data of the individual sensors. In the next step, we plan to harmonize even the intensity values measured by the LiDAR sensors themselves in order to achieve a consistent texture of the point clouds (radiometric calibration). In addition, we continue to work on time-synchronous image-based texturing of the 3D data. A preview of this is given in Video 1, which shows the data acquisition of the scenario "1. urban (curvy path)" with the calibrated MLS system. The synchronously acquired RGB video data were transferred to the 3D points in the overlapping area of the respective fields of view. Video 1 shows the textured 3D sensor data of the previous 10 seconds, whereby a CAD model of the sensor vehicle MODISSA is placed to its actual position. Finally, we would like to point out that sensor data of the presented sensor system are made available on the internet[26].

Video 1. Mobile acquisition of textured 3D point clouds. To watch the video: http://dx.doi.org/10.1117/12.2556476

REFERENCES

[1] Anguelov, D., Dulong, C., Filip, D., Frueh, C., Lafon, S., Lyon, R., Ogale, A., Vincent, L., Weaver, J., "Google Street View: Capturing the World at Street Level," IEEE Computer 43 (6), 32-38 (2010).

[2] Schenk, T., "Modeling and Analyzing Systematic Errors in Airborne Laser Scanners," Technical Notes in Photogrammetry 19, Ohio State University, Columbus, OH., 42 p (2001).

[3] Filin, S., "Recovery of Systematic Biases in Laser Altimetry Data Using Natural Surfaces," Photogrammetric Engineering and Remote Sensing 69 (11), 1235-1242 (2003).

[4] Shan, J., Toth, C. K., [Topographic Laser Ranging and Scanning], CRC Press, Boca Raton, FL. (2009).

[5] Levinson, J. S., "Automatic Laser Calibration, Mapping, and Localization for Autonomous Vehicles," Ph.D. Thesis, Stanford University, Stanford, CA. (2011).

[6] Nüchter, A., Lingemann, K., Hertzberg, J., Surmann, H., "6D SLAM - Mapping Outdoor Environments," Journal of Field Robotics 24 (8-9), 699-722 (2007).

[7] Hebel, M., Stilla, U., "Simultaneous Calibration of ALS Systems and Alignment of Multiview LiDAR Scans of Urban Areas," IEEE Transactions on Geoscience and Remote Sensing 50 (6), 2364-2379 (2011).

[8] Maas, H.-G., "Methods for Measuring Height and Planimetry Discrepancies in Airborne Laserscanner Data," Photogrammetric Engineering & Remote Sensing 68 (9), 933-940 (2002).

[9] Ressl, C., Kager, H., Mandlburger, G., "Quality Checking of ALS Projects Using Statistics of Strip Differences," International Archives of Photogrammetry, Remote Sensing and Spatial Information Sciences 37 (3b), 253-260 (2008).

[10] Vosselman, G., "Analysis of Planimetric Accuracy of Airborne Laser Scanning Surveys," International Archives of Photogrammetry, Remote Sensing and Spatial Information Sciences 37 (3a), 99-104 (2008).

[11] Kager, H., "Discrepancies Between Overlapping Laser Scanner Strips," International Archives of Photogrammetry, Remote Sensing and Spatial Information Sciences 35 (B/1), 555-560 (2004).

[12] Habib, A., Kersting, A. P., Bang, K. I., Lee, D.-C., "Alternative Methodologies for the Internal Quality Control of Parallel LiDAR Strips," IEEE Transactions on Geoscience and Remote Sensing 48 (1), 221-236 (2010).

[13] Soudarissanane, S. S., van der Sande, C. J., Khoshelham, K., "Accuracy Assessment of Airborne Laser Scanning Strips Using Planar Features," Proceedings of the International Calibration and Orientation Workshop EuroCOW 2010, Castelldefels, Spain, 6 p (2010).

[14] Hillemann, M., Weinmann, M., Mueller, M. S., Jutzi, B., „Automatic Extrinsic Self-Calibration of Mobile Mapping Systems Based on Geometric 3D Features," Remote Sensing 11 (16), 1955, 29 p (2019).

[15] Hillemann, M., Meidow, J., Jutzi, B., „Impact of Different Trajectories on Extrinsic Self-calibration for Vehicle-based Mobile Laser Scanning Systems," International Archives of Photogrammetry, Remote Sensing and Spatial Information Sciences 42 (2/W16), 119-125 (2019).

[16] Ressl, C., Mandlburger, G., Pfeifer, N., "Investigating Adjustment of Airborne Laser Scanning Strips Without Usage of GNSS/IMU Trajectory Data," International Archives of Photogrammetry, Remote Sensing and Spatial Information Sciences 38 (3/W8), 195-200 (2009).

[17] Habib, A., Kersting, A., Bang, K., "Impact of LiDAR System Calibration on the Relative and Absolute Accuracy of the Adjusted Point Cloud," Proceedings of the International Calibration and Orientation Workshop EuroCOW 2010, Castelldefels, Spain, 6 p, (2010).

[18] Skaloud, J., Lichti, D., "Rigorous Approach to Bore-sight Self-calibration in Airborne Laser Scanning," ISPRS Journal of Photogrammetry and Remote Sensing 61 (1), 47-59 (2006).

[19] Rieger, P., Studnicka, N., Pfennigbauer, M., "Boresight Alignment Method for Mobile Laser Scanning Systems," Journal of Applied Geodesy 4 (1), 13-21 (2010).

[20] Glennie, C., "Calibration and Kinematic Analysis of the Velodyne HDL-64E S2 Lidar Sensor," Photogrammetric Engineering & Remote Sensing 4, 339-347 (2012).

[21] Borgmann, B., Schatz, V., Kieritz, H., Scherer-Klöckling, C., Hebel, M., Arens, M., "Data Processing and Recording Using a Versatile Multi-sensor Vehicle," ISPRS Annals of the Photogrammetry, Remote Sensing and Spatial Information Sciences 4 (1), 21-28 (2018).

[22] Diehm, A. L., Hammer, M., Hebel, M., Arens, M., "Mitigation of Crosstalk Effects in Multi-LiDAR Configurations," Electro-Optical Remote Sensing XII, Proceedings of the International Society for Optics and Photonics (SPIE) Vol. 10796, 1079604 (2018).

[23] Borgmann, B., Hebel, M., Arens, M., Stilla, U., "Using Neural Networks to Detect Objects in MLS Point Clouds Based on Local Point Neighborhoods," ISPRS Annals of the Photogrammetry, Remote Sensing and Spatial Information Sciences 4 (2/W7), 17-24 (2019).

[24] Hammer, M., Hebel, M., Laurenzis, M., Arens, M., "Lidar-based Detection and Tracking of Small UAVs," Unmanned Sensors and Systems and Countermeasures II, Proceedings of the International Society for Optics and Photonics (SPIE) Vol. 10799, 10799S (2018).

[25] Gehrung, J., Hebel, M., Arens, M., Stilla, U., "An Approach to Extract Moving Objects from MLS Data Using a Volumetric Background Representation," ISPRS Annals of the Photogrammetry, Remote Sensing and Spatial Information Sciences 4 (1/W1), 107-114 (2017).

[26] Hebel, M., Gehrung, J., "The *TUM City Campus* mobile laser scanning test data sets", Fraunhofer IOSB, http://s.fhg.de/mls1 (18 April 2016) and http://s.fhg.de/mls2 (19 December 2018).